THE JOURNAL OF PHYSICAL CHEMISTRY C

pubs.acs.org/JPCC Article

Mechanism and Effects of Coverage and Particle Morphology on Rh-Catalyzed NO−H_2 Reactions

Pavlo Kravchenko, Varun Krishnan, and David Hibbitts*

Cite This: J. Phys. Chem. C 2020, 124, 13291−13303 Read Online

ACCESS | Metrics & More | Article Recommendations | Supporting Information

ABSTRACT: Three-way catalysts, which typically include Rh, are used to treat automotive exhaust and reduce nitric oxide (NO) with a combination of CO and H_2, although few kinetic and theoretical investigations have studied NO−H_2 reactions on Rh. Here, we examine NO activation, which is believed to control the rate of NO reduction, through direct, NO-assisted, and H_2-assisted dissociation pathways on NO*-covered Rh(111) surfaces and Rh nanoparticle models using density functional theory (DFT) and contrast these results with previously reported data on Pt(111) surfaces. Saturation coverages—determined by incrementally adsorbing NO*—were determined to be 5/9 ML NO* on Pt(111), 6/9 ML on Rh(111), and 1.38 ML on a 201-atom Rh nanoparticle (~2 nm). Free energies of activation and reaction were calculated by DFT for the pathways at these coverages and interpreted through maximum rate analyses over a wide range of NO and H_2 pressures to predict NO activation mechanisms and kinetics. Rates are inhibited by NO at all relevant NO pressures and to similar extents on all catalyst models. On Pt(111) surfaces, NO is activated through NOH* formation and dissociation (to N* and OH*) at low H_2 pressures (<0.5 bar) and through HNOH* (to HN* and OH*) at high H_2 pressures (>0.5 bar), resulting in a shift in the H_2 dependency from half order to first order. NO is activated through NOH* formation and dissociation on Rh(111) at all relevant H_2 pressures, with all other pathways being >1000 times slower. NO activation occurs with similar rates through either NOH* or HNO* on Rh particles at 1.38 ML NO*, indicating that these high coverages can shift mechanistic preferences. Predicted NO consumption rates are half order in H_2 on Rh particles and surfaces and are similar in magnitude to one another, despite shifts in the mechanism; these rates on Rh are 10^6 times slower than Pt, consistent with the prior reports that demonstrate that equal turnover rates for Pt at 60 °C occur for Rh at 200 °C. This work demonstrates that strong N═O bonds activate through bimolecular (assisted) pathways and that particle models of catalysts enable high coverages of strongly bound species, which can then influence relative rates and mechanistic predictions.

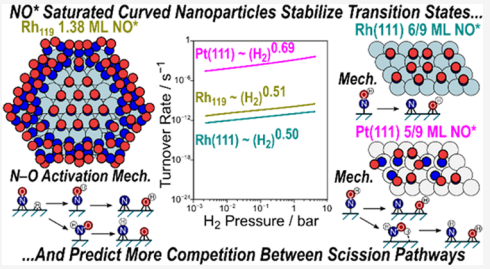

1. INTRODUCTION

Nitric oxide (NO) is an undesirable constituent of automotive exhaust that is removed from exhaust streams from stoichiometric engines using three-way catalysts. These catalysts contain supported clusters of Pd, Pt, and Rh on various oxide supports[1−4] and convert NO, CO, and uncombusted hydrocarbons into N_2, CO_2, and H_2O. NO can be reduced on these catalysts by H_2, CO, NH_3, or hydrocarbons;[2,5−8] however, these catalysts are insufficiently reactive at low temperatures (<600 K),[9] resulting in uncontrolled emissions during automotive startup. Rh is a commonly used catalyst in automotive treatments because it exhibits higher reactivity toward NO_x reduction (by CO or hydrocarbon reductants) in automotive exhaust streams than other Pt-group metals.[10,11] H_2, however, is another possible reductant that can be formed from the dehydrogenation of hydrocarbons or by the water gas shift reaction. In the case of NO reduction by H_2, Rh is less reactive than Pt or Pd.[12,13] NO reduction with H_2 occurs at temperatures above 433 K at NO pressures of 3−24 mbar and H_2 pressures of 12−120 mbar on Pt-group metals.[14,15] At low temperatures (<473 K), undesirable N_2O and NH_3 side products are formed and do not decompose.[15] Understanding the mechanisms and processes that limit NO−H_2 reactions on Rh are necessary for the development of more active catalysts to meet ever-growing emission standards.[16]

Several reports[4,17−22] have proposed that NO dissociation occurs directly through reaction with a vacant site (*) on metal surfaces

$$NO^* + * \rightarrow N^* + O^* \quad (1)$$

The newly formed N* can either combine with other adsorbed N* species to form N_2, combine with NO* to form N_2O, or combine with H* to ultimately form NH_3. Indeed, direct dissociation of NO* is observed during surface science studies on Rh(111) at low NO* coverages (<0.5 ML).[23] NO*

Received: May 5, 2020
Revised: May 22, 2020
Published: May 25, 2020

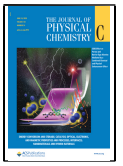

https://dx.doi.org/10.1021/acs.jpcc.0c04024
J. Phys. Chem. C 2020, 124, 13291−13303

dissociation is self-inhibiting[23] as NO* coverage increases, suggesting that direct dissociation only occurs with isolated NO*. Under relevant catalytic conditions (443 K, P_{NO} = 4.5−24 mbar, P_{H_2} = 12−120 mbar), the Rh surface is saturated by NO*, as observed by in situ Fourier transform infrared (FTIR) measurements.[15] Additionally, this direct dissociation mechanism does not directly explain first-order H_2 dependence on NO consumption rates on Pt and half-order H_2 dependence on Rh catalysts at relevant pressures.[14,15] This H_2 dependence implies that H-atoms are involved in the dissociation of NO* or remove site-blocking intermediates. A mechanism consistent with the first-order H_2 dependence on Pt catalysts involves H-assisted NO dissociation in which H first weakens the strong N═O bond by forming NOH* or HNO* species on the catalyst surface

$$NO^* + H^* \rightarrow NOH^* \quad (2)$$

$$NO^* + H^* \rightarrow HNO^* \quad (3)$$

followed by further hydrogenation to HNOH*

$$NOH^* + H^* \rightarrow HNOH^* \quad (4)$$

$$HNO^* + H^* \rightarrow HNOH^* \quad (5)$$

requiring a total of two H* atoms. If the formation or dissociation of *HNOH* is kinetically relevant, then a first-order dependence in H_2 on a NO*-covered surface would result, as observed for Pt at H_2/NO ratios < 1000 where H* is not an abundant surface intermediate. These hydrogenated NH_xOH_y* species can then cleave to form N*, NH_x*, O*, and OH* species, which can subsequently react with one another and NO* or H* to form all observed products.

Despite the ubiquity of Rh in automotive catalysis,[11] few kinetic studies on supported Rh catalysts have been performed for NO−H_2 reactions. Surface science studies on Rh(111) and Rh(533) surfaces have demonstrated oscillatory kinetics,[24−26] and that the concentrations of products are out of phase with the reactants. These results suggest that NO−H_2 reactions are limited by the desorption of products or removal of site-blocking species (e.g., N* or O*). These oscillations are not present at high pressures on supported Rh catalysts. Exposing a Rh(111) surface covered in NO* with a H_2 atmosphere results in the desorption of NO* followed by H_2 adsorption in the newly formed vacancy and subsequent reaction with NO* to form NH_x* species.[27] Observations at catalytic conditions on supported Rh indicate that the consumption of NO and formation rates of every observed product (N_2O, N_2, and NH_3) are promoted by H_2 (at 443 K, P_{NO} = 4.5−24 mbar, P_{H_2} = 12−120 mbar); a half-order H_2-dependence is observed for NO consumption, N_2O and N_2 formation, and between half- and first-order H_2 dependence for NH_3,[15] suggesting that H-assisted NO dissociation routes may dominate over direct routes or that H_2 decreases the coverage of site-blocking species. A higher-order H_2 dependence for NH_3 formation indicates that branching points in the formation of NH_3 vs N_2 and N_2O products are H_2-dependent, while the ratio of N_2 to N_2O is independent of NO and H_2 pressure on both Rh and Pt catalysts.[15,20,28] These impacts of reactant pressure on product formation rates indicate that all products are formed from NO and H_2 through a common intermediate, with N* being previously proposed based on transient experiments examining Pt/Al_2O_3.[20] NO inhibits NO−H_2 rates on Rh, but only to the −0.2 order,[15] in contrast to Pt where NO inhibits with orders of −1 at high NO* coverage.[14] Dinitrosyl complexes (such as ONNO*) are observed with in situ IR measurements at lower temperatures (∼300 K) and these peaks quickly disappear above 423 K, possibly reflecting the formation of N_2O from preadsorbed NO on Rh through NO-assisted N−O dissociation reactions.[29] These kinetic data offer both direct and indirect evidence of NO−H_2 reaction routes in the absence of direct theoretical investigations of this reaction.

Previous density functional theory (DFT) studies on bare Rh(111) and (221) surfaces suggest that direct dissociation of NO is the most favorable route.[30] This is consistent with the observation of dissociative adsorption of NO at low coverages NO*.[23] These bare surface results, however, neglect coverage effects, which can significantly alter reaction rates and preferred mechanisms. Additional mechanistic insights can be drawn from DFT studies on other platinum group metals. Theoretical investigations on Pd(211) surfaces show that NO* activates through H_2-assisted pathways to form HNOH* at higher temperatures (>500 K), while at low temperatures, H_2 scavenges O* to create empty sites where NO* can then react via NO-assisted pathways to form ONNO* that decomposes into N_2 through N_2O.[31] Theoretical investigations on Pt(100) and (111) surfaces suggest that at low coverage and low H_2 pressure, NO* activates directly,[22] consistent with surface science observations,[23] but H-assisted routes dominate when co-adsorbed NO is present. Mechanistic investigations employing maximum rate analyses suggest that the kinetically relevant step in covered Pt(111) surfaces involves N−O scission and that the removal of site-blocking intermediates, such as N* or O*, by H_2 is facile.[32] The relative rates of H-assisted routes on Pt(111), such as dissociation through NOH* or HNOH*, depend on the coverage of spectating species.[14] H-assisted routes occur with lower activation barriers,[14] indicating that direct routes are only feasible at low H_2 pressures. These studies suggest that there are three possible ways NO activates during NO−H_2 reactions: a direct route where NO* cleaves directly and H_2 acts as an O* scavenger, a NO*-assisted route, which forms N_2 and N_2O through ONNO*, or H-assisted routes via hydrogenation reactions (eqs 2−5), which precede N−O dissociation; these three routes are examined in this study.

Bare or partially covered periodic surface models are commonly used to model catalytic reactions. These models, however, do not accurately capture co-adsorbate interactions, and the periodic nature of surface models can result in artifacts that overpredict barriers for reactions with positive activation areas.[33] Additionally, undercoordinated metal atoms, such as single-atom[34,35] catalysts, or defects and edges of curved nanoparticles can bind multiple adsorbates (previously demonstrated for CO* or H*),[33,36,37] leading to supra-monolayer coverages in conjunction with nanoparticle terrace saturation. The curvature of the particle therefore influences both the coverage of abundant surface intermediates as well as the site requirements for catalytic reactions (and thus their predicted turnover rates and kinetic behavior). The role of particle curvature has not yet been investigated for NO* reduction and should be critical as these reactions occur at high NO* coverages at even ppm levels of NO.

In this work, we assess direct, NO-assisted, and H-assisted NO cleavage pathways at 1.38 ML NO* on Rh_{119} hemispherical nanoparticle models and contrast these results with the periodic surface Rh(111) model at 6/9 ML NO*. Additional comparisons are made to Pt(111), which has been previously described in detail.[14,32] Particle models result

https://dx.doi.org/10.1021/acs.jpcc.0c04024
J. Phys. Chem. C 2020, 124, 13291−13303

in lower barriers for reactions with negative activation areas, as the crowded NO* adlayer is allowed to relax, while larger transition states are destabilized by dense NO* adlayers resulting in larger barriers than those on surface models. Predicted rates on both Rh_{119} and Rh(111) models are similar in magnitude, but the mechanism and rate-determining steps predicted by the two DFT models differ, indicating the importance of particle models to obtain accurate assessments of high-coverage reactions.

2. COMPUTATIONAL METHODS

Periodic plane-wave density functional theory (DFT) calculations were run using the Vienna ab initio simulation package (VASP)[38−41] implemented in the computational catalysis interface (CCI).[42] Plane waves were constructed using projector-augmented wave (PAW) potentials with an energy cutoff of 400 eV.[43,44] The revised Perdew−Burke−Ernzerhof (RPBE) form of the generalized gradient approximation (GGA) was used to determine exchange-correlation energies.[45−47] Optimization calculations were performed in two steps, with both steps optimizing the structures until the force on any atom was <0.05 eV $Å^{-1}$. In the first step, wave functions were converged to within 10^{-4} eV and forces were calculated using a fast Fourier transform (FFT) grid of 1.5× the plane-wave cutoff. In the second step, wave functions were converged to within 10^{-6} eV and forces were calculated using a FFT grid 2× the plane-wave cutoff, with geometries then converged with these settings, which provide more accurate forces. Surface calculations were converged with a 4 × 4 × 1 Monkhorst−Pack sampling of the first Brillouin zone during geometric convergence, followed by a single-point calculation at an 8 × 8 × 1 sampling to compute final electronic energies.[48] For particle calculations, the Brillouin zone was sampled at the Γ-point in all calculations and the geometries were (as before) converged in a two-step scheme. These multistep optimization schemes implemented in CCI are 4−7× faster than analogous one-step calculations.[42]

Reaction pathways were estimated using the nudged elastic band (NEB)[49,50] method. NEB calculations used 16 images with wave functions converged to within 10^{-4} eV with a FFT grid of 1.5× the plane-wave cutoff. The maximum force on any atom was <0.5 eV $Å^{-1}$. These pathways provided rough estimates of the transition states that were further refined using the Dimer method,[51] which optimizes a pair of structures to determine local curvature of the potential energy surface, locate saddle points, and compute transition-state energies. Dimer calculations were performed using the same convergence criteria as optimization calculations described above.

Frequency calculations were carried out using a fixed displacement method with two displacements for every intermediate and transition state. For surface calculations, all metal atoms were fixed and all adsorbate atoms (including spectating NO* species) were displaced (vibrated). For particle calculations, atoms in reacting species and NO* on five metal atoms of the (111) terrace were vibrated while all other atoms were fixed. Allowing every atom on every terrace site to relax results in the same activation energies (within 5 kJ mol^{-1}, Figure S1) as this abridged sampling scheme while requiring 4× the computational resources. Low-frequency modes (<60 cm^{-1}) were replaced with 60 cm^{-1}, as done in the previous work,[52−55] because low frequencies are inaccurately determined by DFT methods and contribute significantly to vibrational entropy, but to neglect these modes would underestimate adsorbate entropy. These frequency calculations were used to determine zero-point vibrational energies (ZPVE) and temperature-corrected enthalpies (H) and free energies (G) using harmonic oscillator approximations for vibrational partition functions (see Section S2 of the Supporting Information (SI) for details) and combined with ideal gas treatments (for gas-phase molecules) of rotational and translational partition functions to give enthalpies

$$H = E_0 + \mathrm{ZPVE} + H_{\mathrm{vib}} + H_{\mathrm{trans}} + H_{\mathrm{rot}} \quad (6)$$

and free energies

$$G = E_0 + \mathrm{ZPVE} + G_{\mathrm{vib}} + G_{\mathrm{trans}} + G_{\mathrm{rot}} \quad (7)$$

for all adsorbate, reactant, product, and transition states at 423 K.

Two types of models were considered for this study: surface models and particle models. Surface calculations remain ubiquitous but do not accurately model reactions at high co-adsorbate coverages because artifacts in co-adsorbate interactions arise at high coverages from the periodic nature of these calculations.[56,57] To determine the saturation coverages, surfaces were filled incrementally starting from a bare surface and adding 1 NO to every possible adsorption site. The minimum energy configuration for each intermediate filling was used to calculate a differential binding energy (ΔE_{diff}), which is the binding energy for each stage of filling.i.e.,

$$\Delta E_{\mathrm{diff},i} = E_{\mathrm{NO}^*,i} - E_{\mathrm{NO}^*,i-1} - E_{\mathrm{NO(g)}} \quad (8)$$

where $E_{\mathrm{NO}^*,i}$ is the minimum energy configuration for the surface with i NO*, $E_{\mathrm{NO}^*,i-1}$ is the minimum energy configuration for the surface with one fewer NO*, and $E_{\mathrm{NO(g)}}$ is the energy for NO(g). Differential enthalpies, entropies, and free energies are calculated with the assistance of vibrational frequency calculations as described. Rh_{201} particle models were also incrementally filled to determine saturation coverage; however, instead of one NO adsorption event at a time like the surface case, all symmetrically equivalent sites of one "type" were filled at a time. For example, NO* might be placed at all face-centered cubic (fcc)-terrace sites or at all bridge sites along edge/corner atoms. Then, more NOs were added to whichever type of binding site was the most stable. Calculating every unique configuration across all sites on a Rh_{201} particle would be computationally intractable because of the large number of unique configurations. The differential binding energy is averaged for every new NO* added to the surfacei.e.,

$$\Delta \overline{E}_{\mathrm{diff},i} = \frac{E_{\mathrm{NO}^*,i+x} - E_{\mathrm{NO}^*,i} - xE_{\mathrm{NO(g)}}}{x} \quad (9)$$

where $\Delta \overline{E}_{\mathrm{diff},i}$ is the average differential adsorption energy, i is the number of NO* adsorbed, and x is the number of new NO* added. Free energies were not calculated on the Rh_{201} particle as frequency calculations are computationally intractable with the large number of NO* adsorbed to the particle, so the effects of entropy upon NO* adsorption are estimated based on the surface data. This method of filling a particle surface was previously used to examine H* chemisorption on Pt and Ir particles.[36]

Reactions were modeled on 3 × 3 unit cells of Rh(111) surfaces with four metal layers and a 10 Å vacuum layer (Figure 1). The two bottom-most layers of these surfaces were fixed in their bulk crystallographic positions. Surfaces were

https://dx.doi.org/10.1021/acs.jpcc.0c04024
J. Phys. Chem. C 2020, 124, 13291−13303

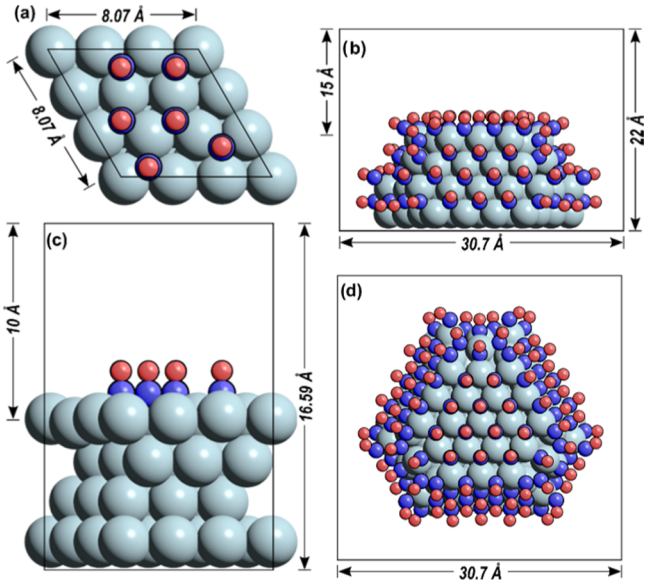

Figure 1. Top-down and side views of the 6/9 ML-covered Rh(111) surface (a and c) and the 1.38 ML NO Rh_{119} half-particle model (b and d). The bottom two metal layers of each were constrained during structural convergence, and all NO* bound to the bottom two layers of the Rh_{119} model were constrained.

calculated with 3−4 spectating NO* species during all reactions (corresponding to a total effective resting-state coverage of 6/9 ML NO*, Figure 1a,c). Converged structures from the Rh surface calculations were transferred using CCI tools to a Rh_{119} half-particle model covered with 84 NO* molecules on all terrace, edge, and corner sites (corresponding to a total coverage of 1.38 ML, Figure 1b,d). To create this Rh_{119} model, a full cubo-octahedral Rh_{201} particle with (111) and (100) terraces was filled incrementally until no more NO* could be added without significant restructuring of the particle or positive NO* adsorption free energies (indicating surface saturation). Once saturated, the particle was cleaved, the bottom two layers of the half particle and all NO bound to those atoms were constrained for all subsequent calculations on the surfaces of that particle. Reactions were only considered to occur on terrace sites as those most closely match the infinite terraces in periodic surface models. While edge sides may participate in the chemistry, undercoordinated sites tend to be more reactive and thus would bind adsorbates such as NO more strongly, requiring more energy to form a vacancy or desorb products. In other words, they are more reactive, but there is a lower probability of encountering a vacant corner or edge site. We will investigate the role of undercoordinated atoms in NO−H_2 chemistry as part of future studies.

3. RESULTS AND DISCUSSION

3.1. Saturation Coverage for Different Models. NO* coverages were varied from 1/9 to 1 ML on Rh(111) 3 × 3 surfaces (Figure 2) and Pt(111) 3 × 3 surfaces in the previous work.[14] NO was incrementally added to every site, and all symmetrically unique adsorbate configurations were considered, including atop, bridge, and both the fcc and hexagonal close-packed (hcp) three-fold hollow sites for NO* as well as mixtures of those binding modes. The minimum free-energy configuration (at 1 bar, 423 K) is discussed here, while Section S3 of the SI provides details for all configurations. NO* adsorption free energies (eq 8) on bare Pt(−67 kJ mol^{-1}) and Rh(−140 kJ mol^{-1}) surfaces are negative (Figure 2) and demonstrate that NO* binds much more strongly to Rh than Pt, as expected by periodic trends of transition metals.[58] NO* adsorption free energies become less favorable as NO* coverage increases because of a combination of through-space and through-surface repulsions that weaken metal-atom binding strength as coverage increases. NO* adsorption free energies remain negative (indicating likely adsorption at 1 bar and 423 K) on Pt(111) until NO* coverages reach 5/9 ML where it increases to +44 kJ mol^{-1}. NO* shifts from three-fold binding sites at low coverage to atop binding sites at high coverage on Pt(111) to minimize metal-atom sharing among co-adsorbates.[14] NO* binds more strongly to Rh than to Pt, but NO* still repels co-adsorbed NO*, leading to positive adsorption free energies at coverages above 6/9 ML. These surface filling calculations indicate that extended (defect-free) Pt and Rh metal surfaces saturate at 5/9 and 6/9 ML NO*, respectively. This is consistent with NO adsorption surface science studies on Rh(111), Rh(110), and Rh(100),[59−61] which suggest saturation coverages of 0.60−0.80 ML (at 100 K, 10^{-5} torr NO).

Supported nanoparticles, typical of practical automotive exhaust catalysts, bind H* and CO* more strongly at high coverages than their surface counterparts because the adlayer is allowed to laterally relax on the curved particles.[33,37,62,63] NO* binds most strongly to corner sites of Rh_{201} particle models and with adsorption energies of −239 kJ mol^{-1} when all such sites are simultaneously filled. This symmetric and block-filling method is not meant to rigorously describe NO* filling as it is computationally intractable to examine every configuration and every coverage on a surface of this size and heterogeneity. Once corner sites are filled, NO* next binds most strongly to

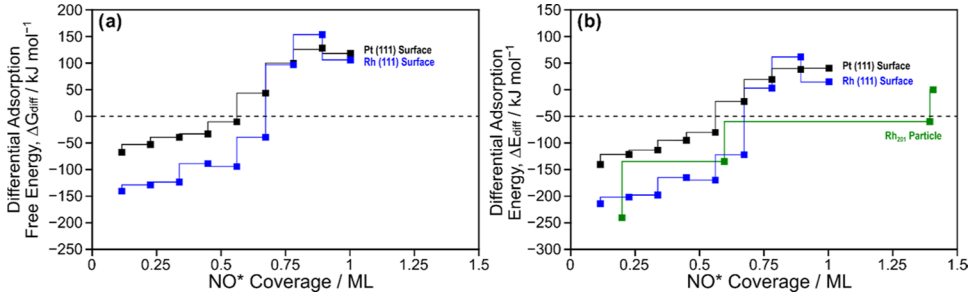

Figure 2. Differential NO adsorption (a) free energies (423 K, 1 bar, ΔG_{diff}) and (b) potential energies (ΔE_{diff}) on a Rh(111) 3 × 3 surface (blue), Pt(111) 3 × 3 surface (black),[14] and Rh_{119} particle (green). Estimated NO* entropies on Rh_{201} particles indicate that $\Delta E_{diff} \sim -50$ kJ mol^{-1} corresponds to $\Delta G_{diff} = 0$, hence the shifted axis. Rh structural images for minimum energy configurations are available in Section S3 of the SI.

https://dx.doi.org/10.1021/acs.jpcc.0c04024
J. Phys. Chem. C 2020, 124, 13291−13303

bridge sites between undercoordinated edge and corner Rh atoms with an average differential adsorption energy of −134 kJ mol^{-1} (where the binding energies are averaged across the additional 48 NO* adsorbates at those sites). NO* then binds to 3-fold hcp sites with an average differential adsorption energy of −58 kJ mol^{-1} to reach a total NO* coverage of 1.38 ML. The adsorption energy of a single NO* on the terrace of the Rh cluster at 1.38 ML NO* is 1 kJ mol^{-1}, indicating that further adsorption is energetically unfavorable.

These adsorption potential energies do not directly give free-energy estimates, and frequency calculations of the full NO* adlayer on the Rh_{201} particle model are computationally intractable. The average adsorption entropies of NO* on Rh(111) surfaces vary weakly from −161 to −175 J mol^{-1} K^{-1} as coverage increases from 1/9 to 1 ML NO*, while the calculated entropy of gas-phase NO at 423 K and 1 bar is 210 J mol^{-1} K^{-1}. Differential adsorption entropies (per NO*) are therefore relatively insensitive to the coverage as values change from −161 to −192 J mol^{-1} K^{-1} on Rh(111) and −162 to −159 J mol^{-1} K^{-1} on Pt(111) surfaces. In lieu of calculating vibrational frequencies and thus estimating adsorbate entropies for NO* on Rh_{201} particles, here we estimate the entropy loss upon NO* adsorption on these particles to be −192 J mol^{-1} K^{-1} because our calculations indicate that the last sites filled are terrace atoms near 1 ML. Using this estimated adsorption entropy, we estimate that Rh_{201} particles saturate at adsorption potential energies less negative than −50 kJ mol^{-1}, indicating that the 1.38 ML NO* model used here (Figure 1b,d) is a reasonable coverage for these small Rh_{201} particles (∼2 nm in diameter).

The desorption free energies of a single NO* on a Pt surface (111) at 5/9 ML, Rh(111) surface at 6/9 ML, and the (111) terrace of the Rh_{119} half particle at 1.38 ML are 9, 40, and 9 kJ mol^{-1}, respectively. Further adsorption is less favorable, indicating that vacancies are scarce during catalysis. These positive desorption free energies indicate that the models are adequately covered with NO at standard pressures, and the larger desorption energy for Rh(111) is a consequence of the model size. Adsorption−desorption events can be considered rapid and quasi-equilibrated. Sufficiently large heterogeneous catalyst surfaces exhibit a continuum of adsorption energies, where adsorption becomes less favorable as coverages increase for large repulsive species, such as NO*. When the coverage-dependent adsorption free energy is 0, then the surface is saturated at 1 bar of that species. Energies to desorb an adsorbate from a large saturated surface depend on gas-phase pressures and should be relatively independent of the catalyst or model—which instead alters the coverage at which saturation occurs. Here, desorption energies for NO* are 9 and 40 kJ mol^{-1} and correspond to coverages of 1.38 ML on the Rh_{201} particle and 6/9 ML NO* on the Rh(111) surface because these models are small. The partially covered 6/9 ML NO Rh(111) surface and fully covered (1.38 ML NO) particle are used as the reference states for the mechanistic analyses in the remainder of this work.

3.2. Energetics of NO Reduction Pathways. Six NO* scission pathways were considered in this work (Scheme 1). NO and H_2 adsorption−desorption is assumed to be quasi-equilibrated for all pathways. NO* can dimerize with a neighboring NO* to form an ONNO* complex. This complex then decomposes to N_2O and O* on the surface (pathway 1). For all of the other pathways, one NO* must desorb and form a vacancy on the surface, consistent with NO inhibition on Pt and Rh catalysts.[14,15] NO* can then react with this vacancy to cleave directly (pathway 2) or hydrogenate either to HNO* (pathway 3) or NOH* (pathway 4) and then dissociate. Alternatively, HNO* or NOH* can be hydrogenated to HNOH*, which then cleaves to HN* and OH* (pathway 5), which was determined to be the mechanism of NO* activation on Pt catalysts from a combination of kinetic, isotopic, and theoretical data.[14] Further hydrogenation to H_2NOH* and subsequent cleavage to H_2N* and OH* (pathway 6) are also considered.

Scheme 1. Reaction Scheme for Direct (Pathways 1 and 2) and H-Assisted (Pathways 3−6) NO Scission Routes[a]

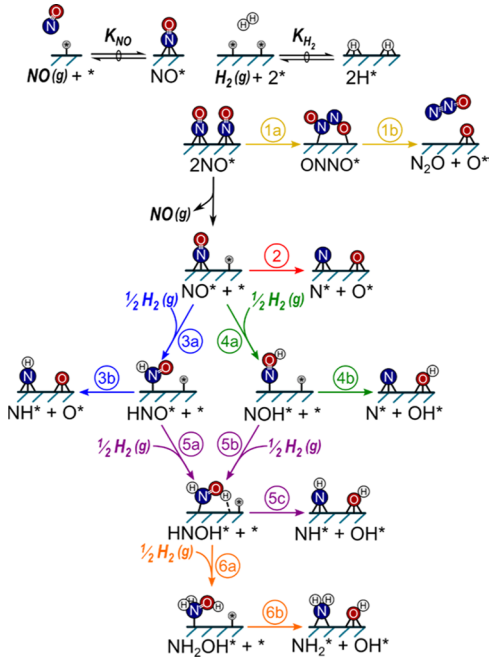

[a]Breaking the N−O bond can be assisted by co-adsorbed NO* through an ONNO* intermediate or assisted by H* through NOH*, HNO*, HNOH*, or H_2NOH* intermediates.

Rate laws associated with pathways 1 and 2 do not seem to match H_2 pressure dependences observed for Rh (half order in H_2) and Pt (half to first order in H_2) as they do not directly involve H_2, thus requiring H_2 involvement in the removal of potentially site-blocking intermediates such as O* if these are the predominant pathways.[14,15] A half-order dependence on H_2 is observed for Rh systems[15] and this would be expected if pathways 3 or 4 dominate, as one H atom would have to adsorb before the kinetically relevant step (likely N−O dissociation). Similarly, rates are first order in H_2 on Pt, consistent with pathway 5.[14] A 1.5-order dependence in H_2 would be observed if pathway 6 was the dominant pathway and was limited by step 6a or 6b (i.e., NH_2OH* formation or dissociation), but no superlinear H_2 dependence has been observed on Rh or Pt catalysts. In the sections that follow, we compare each catalyst model for various reaction mechanisms (e.g., Section 3.2.1 discusses direct NO* dissociation on all three models); Section S4 in the SI, in contrast, reorganizes the data to compare all mechanisms on each catalyst model individually.

3.2.1. Direct and NO-Assisted NO* Activation.* The six pathways in Scheme 1 were investigated on Rh(111) 3 × 3 surfaces and the (111) terrace on Rh_{119} half-particle models.

https://dx.doi.org/10.1021/acs.jpcc.0c04024
J. Phys. Chem. C 2020, 124, 13291−13303

NO*-assisted NO* activation (pathway 1) routes occur on Pt with an effective barrier of 190 kJ mol^{-1} to dissociate the complex (Figure 3). The overall barriers for this ONNO* dissociation are higher on Rh(111) than on Pt, with a barrier of 222 kJ mol^{-1} to form the ONNO* complex and 285 kJ mol^{-1} to dissociate to N_2O and O*, largely because the ONNO* complex itself is ~80 kJ mol^{-1} less stable on Rh(111) than on Pt(111) at their respective NO* coverages. The decomposition of ONNO* is the difficult step for all three catalyst models, and this reaction occurs with much higher effective barriers on Rh_{119} particles (317 kJ mol^{-1}) than on Rh(111) surface models (285 kJ mol^{-1}). ONNO* decomposition has a positive activation area, where the transition state occupies more space than the reactant state, resulting in increased adlayer strain that is not present on surface models, which saturate at lower coverages and are less crowded than nanoparticles (Figure 4b,f). This concept is analogous to activation volume and was previously used to explain trends in CO* activation on Fischer–Tropsch synthesis[37] and ethane hydrogenolysis[33] reactions. These large barriers indicate that N_2O products are not formed via this route, consistent with the theory that N_2 and N_2O are formed through a common intermediate after N–O scission.[20] Dinitrosyl complexes might not form on Rh terraces and could instead only form on undercoordinated sites—a possibility that will be explored in future studies.

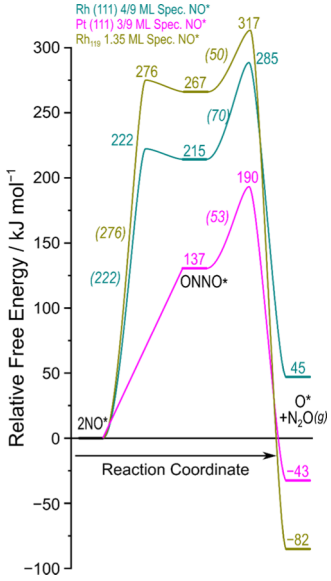

Figure 3. NO*-assisted route for the dissociation of NO* on Pt(111) surfaces (in pink, from ref 14), Rh(111) surfaces (teal), and the (111) terrace on Rh_{119} particles (olive). Intrinsic forward barriers are in parentheses. The coverages during the initial state, denoted by 2 NO*, are 5/9, 6/9, and 1.38 ML NO* for Pt(111), Rh(111), and Rh_{119}, respectively. Free energies are calculated at 423 K, 1 bar NO.

Direct scission of NO* (pathway 2) occurs with barriers of 281 kJ mol^{-1} for Rh surfaces, 248 kJ mol^{-1} for Pt surfaces, and 221 kJ mol^{-1} for Rh_{119} particles (Figure 5). The barrier is lower on Rh_{119} partly because of the high NO* coverage (1.38 ML), which creates strain in the adlayer that can be released by reactions that have a negative activation area. The N–O dissociation transition state (Figure 4c,g) occupies less space than the pair of NO* that it replaces (the reference state in Figure 4a,e); therefore, the relaxation in the adlayer that occurs during NO* activation lowers the NO* activation barrier compared to the flat Rh(111) surface model at 0.67 ML NO* on which the adlayer does not relax.

3.2.2. H-Assisted NO Activation. H-assisted routes require H* to adsorb in a vacancy before NO* can be hydrogenated. H* adsorption free energies are similar across all systems: 17, 13, and 16 kJ mol^{-1} for Rh(111) at 5/9 ML NO*, Pt(111) at 4/9 ML NO*, and Rh_{119} at 1.35 ML NO*, respectively. These unfavorable H* adsorptions reflect repulsive co-adsorbate interactions between H* and NO*. These results, along with the adsorption free energies for NO* at similar coverages (−9

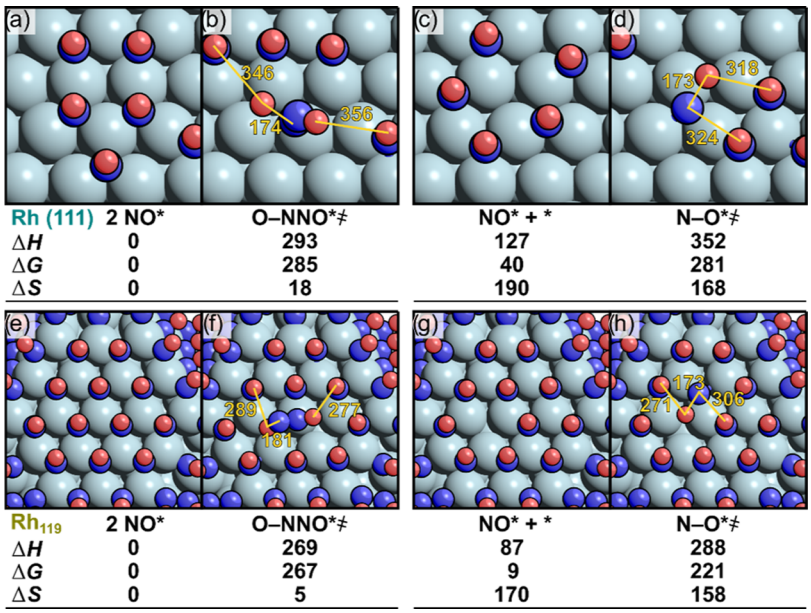

Figure 4. Structural images and enthalpies, free energies (both kJ mol^{-1}), and entropies (J mol^{-1} K^{-1}) to form these states and transition states (‡) from a pair of NO* (the "reference state", parts a, e) at 423 K and 1 bar and 4/9 and 1.35 ML of spectating NO* on Rh(111) (parts a–d) and Rh_{119} (parts e–h), respectively. Relevant distances are labeled in pm. View tilted 10° off the normal vector.

https://dx.doi.org/10.1021/acs.jpcc.0c04024
J. Phys. Chem. C 2020, 124, 13291–13303

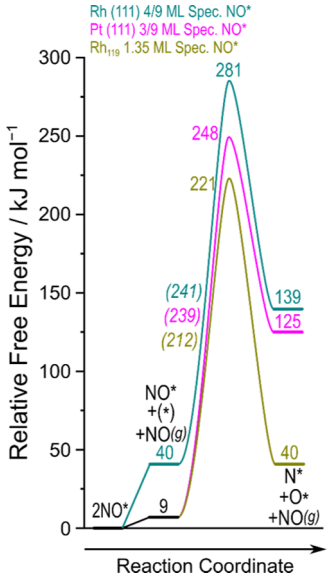

Figure 5. Direct route for the dissociation of NO* on Pt(111) surfaces (in pink, from ref 14), Rh(111) surfaces (teal), and the (111) terrace on Rh_{119} particles (olive). Intrinsic forward barriers are in parentheses. The coverages of the initial states, denoted by 2 NO*, are 5/9, 6/9, and 1.38 ML NO* for Pt(111), Rh(111), and Rh_{119}, respectively. Free energies are calculated at 423 K, 1 bar NO.

to −40 kJ mol^{-1}, Figure 6), indicate that H* coverages would be negligible compared to NO* coverages except at very large

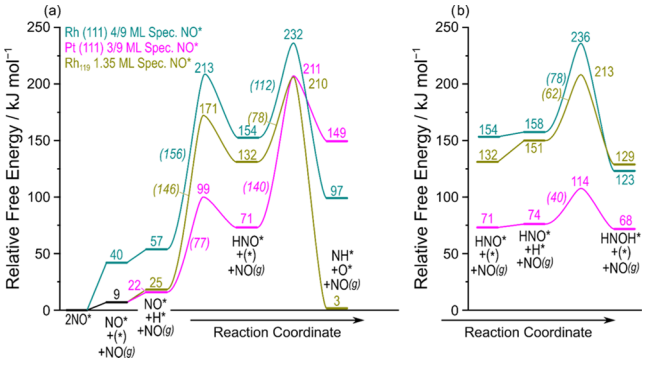

Figure 6. Comparison of (a) HNO* formation, cleavage, and (b) hydrogenation pathways on Pt(111) (in pink, from ref 14), Rh(111) (teal), and Rh_{119} (olive). Intrinsic barriers are in parentheses. The coverages of the initial states, denoted by 2 NO*, are 5/9, 6/9, and 1.38 ML NO* for Pt(111), Rh(111), and Rh_{119}, respectively. Free energies are calculated at 423 K, 1 bar NO and H_2.

H_2/NO ratios (>10^4). Hydrogenation of NO* to HNO* and NOH* is endothermic on all catalyst models and proceeds with lower free-energy barriers on Pt(111) (77 and 72 kJ mol^{-1}, respectively) than on both Rh(111) (156 and 172 kJ mol^{-1}) and Rh_{119} (146 and 185 kJ mol^{-1}) models (Figures 6a and 7a). Intrinsic barriers for HNO* and NOH* dissociation are larger (140 and 86 kJ mol^{-1}) than hydrogenation barriers to form them (77 and 72 kJ mol^{-1}) on Pt(111), while their dissociation occurs with lower intrinsic barriers (78−131 kJ mol^{-1}) than their formation (146−156 kJ mol^{-1}) on Rh catalysts. Structures of relevant transition states indicate that spectating NO* species move into nearby vacancies if reacting species approach during reactions modeled at the intermediate coverages (3/9 and 4/9 ML of spectators) on the Pt and

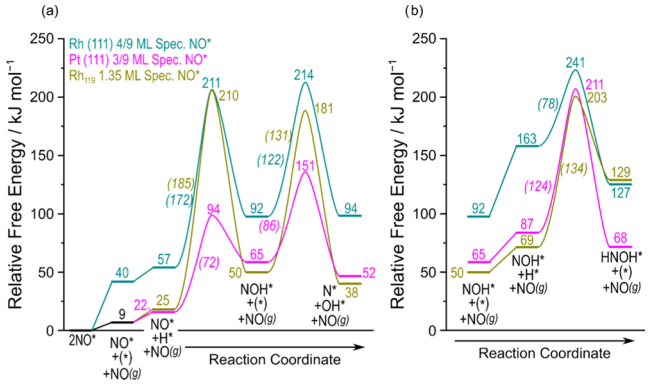

Figure 7. Comparison of (a) NOH* formation, cleavage, and (b) hydrogenation pathways on Pt(111) (in pink, from ref 14), Rh(111) (teal), and Rh_{119} (olive). Intrinsic barriers in parentheses. Intrinsic forward barriers are in parentheses. The coverages during the initial state, denoted by 2 NO*, are 5/9, 6/9, and 1.38 ML NO* for Pt(111), Rh(111), and Rh_{119}, respectively. Free energies are calculated at 423 K, 1 bar NO.

Rh(111) surfaces. This ability of species to reorganize is somewhat unrealistic, as real coverages are likely to be closer to 1 ML than these intermediate coverages. The adlayer on the Rh particles, while mobile, does not have large amounts of empty space where species can reorganize and thus accurately penalizes reactions requiring such reorganization.

HNO*, once formed, can further hydrogenate to form *HNOH* or dissociate to form NH* and O*. On Pt(111), further hydrogenation occurs with much lower barriers (40 kJ mol^{-1}) than dissociation (140 kJ mol^{-1}) and on Rh(111) there is a slight preference for hydrogenation (78 vs 112 kJ mol^{-1}), indicating that Pt is a better hydrogenation catalyst. On the Rh_{119} particle, the large positive H* adsorption free energy (+19 kJ mol^{-1}) near HNO* results in a larger effective barrier for forming *HNOH* (213 kJ mol^{-1}) than for dissociating HNO* (210 kJ mol^{-1}), indicating that the latter may be preferable. However, effective barriers do not correspond to relative rates at all conditions, and only predicted rates at a range of conditions (e.g., from maximum rate analysis, Section 3.3) can discriminate between pathways.

NOH* is more stable than HNO* on all three catalyst models, particularly on Rh_{119} as the higher NO* coverage facilitates H-bond (169 pm) formation between NOH* and a neighboring NO*, shorter than that on Rh(111) surfaces at lower coverage (178 pm), as shown in Figure 8. This leads to higher intrinsic barriers for NOH* dissociation on Rh_{119} (131 kJ mol^{-1}) than on Rh(111) (122 kJ mol^{-1}) but lower effective barriers (181 kJ mol^{-1} on Rh_{119} and 214 kJ mol^{-1} on Rh(111), referenced to a NO*-saturated surface) (Figure 7a). NOH* hydrogenation to form HNOH* occurs with similar energies on both the Pt(111) and Rh_{119} catalyst models, while the relative instability of NOH* and the NOH* + H* state renders NOH* hydrogenation difficult on the Rh(111) surface, as shown in Figure 7b. For all three catalyst models, NOH* dissociation has a lower effective barrier than NOH* hydrogenation, although the difference in the H_2-pressure dependence means that their relative rates will depend on H_2 pressure, as discussed in Section 3.3.

There are two possible routes once HNOH* is formed. Dissociation of HNOH* (step 5c) occurs on Rh(111) and Pt(111) surfaces with effective barriers of 146 and 149 kJ mol^{-1}, respectively (Figure 9a), while on Rh_{119}, the barrier is

https://dx.doi.org/10.1021/acs.jpcc.0c04024
J. Phys. Chem. C 2020, 124, 13291−13303

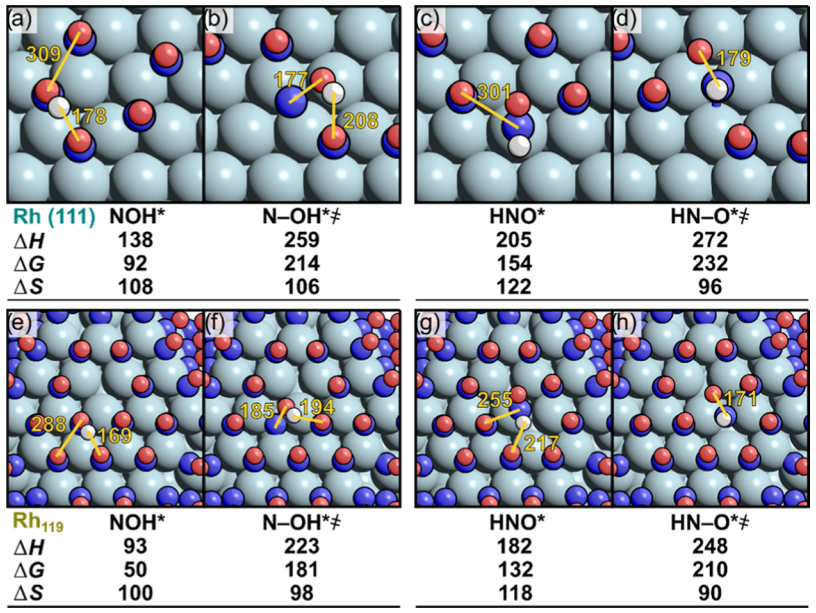

Figure 8. Relative stabilities and structures of (a, e) NOH*, (b, f) N−OH* dissociation transition states, (c, g) HNO*, and (d, h) HN−O* dissociation transition states on Rh(111) surfaces and Rh_{119} particles. Breaking bond and nearest neighbor distances labeled with distances in pm. Free energies and enthalpies in kJ mol^{-1} and entropies in J mol^{-1} K^{-1}, calculated at 423 K 1 bar and referenced to the NO*-saturated model (6/9, 5/9, and 1.38 ML NO* for Rh(111), Pt(111), and Rh_{119}, respectively). View tilted 10° off the normal vector. Additional structural images for hydrogenation steps are available in the SI.

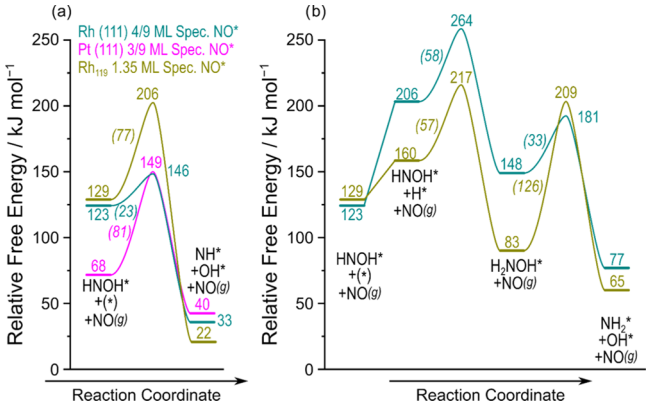

Figure 9. (a) Dissociation of NO* through HNOH* and H_2NOH* on Pt(111) surfaces (in pink, from ref 14), Rh(111) surfaces (teal), and the (111) terrace on Rh_{119} particles (olive). Intrinsic forward barriers in parentheses. The coverage of the initial state, denoted by 2 NO*, is 5/9, 6/9, and 1.38 ML NO* for Pt(111), Rh(111), and Rh_{119}, respectively. Free energies calculated at 423 K, 1 bar.

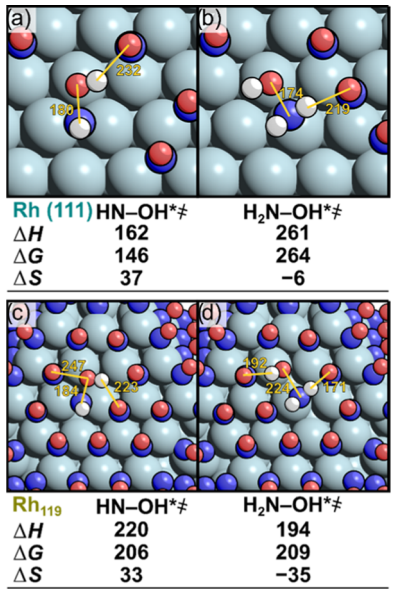

Figure 10. Structural images and enthalpies, free energies, and entropies of dissociation transition states for HNOH* on (a) Rh(111) and (c) Rh_{119} and H_2NOH* on (b) Rh(111) and (d) Rh_{119}. Breaking bonds and nearest neighbor distances are labeled with distances in pm. Free energies and enthalpies are in kJ mol^{-1} and entropies in J mol^{-1} K^{-1}, calculated at 423 K and 1 bar NO and H_2 and referenced to a NO*-saturated model. View tilted 10° off the normal vector. Additional structural images of HNOH*, H_2NOH* formation, and H_2NOH* are available in the SI.

206 kJ mol^{-1} because this *HNOH* formation and dissociation pathway creates strain in the NO* adlayer, which is absent at the relatively low coverages of the surface models (Figure 10a,c). Additionally, OH*−NO* distances (223 pm on Rh_{119}, 232 pm on Rh(111), Figure 10) are long, indicating that H-bonding with the leaving OH* species is weak in these transition states. Hydrogenation barriers to form NH_2OH* are less favorable than *HNOH* dissociation on both Rh models (Figure 9b) (this pathway has not been previously published on Pt), indicating that we have sufficiently hydrogenated NO* to identify reasonable N−O dissociation paths and that other possible routes resulting in supralinear H_2 dependencies are unlikely.

3.3. Maximum Rate Analysis of DFT-Derived Energies. Maximum rate analysis was performed here to determine the reversibility and kinetic relevance of individual elementary steps and which pathway(s) lead to observed rates at pressures and temperatures relevant to NO−H_2 reactions. The maximum rate for each elementary step is computed by assuming that every preceding step is quasi-equilibrated. Each step of the mechanism must be considered separately, and the

https://dx.doi.org/10.1021/acs.jpcc.0c04024
J. Phys. Chem. C 2020, 124, 13291−13303

step with the lowest maximum rate within a series of reactions is the kinetically relevant step of that pathway. Cleaving HNOH* formed via HNO*, for example, would require adsorbing NO and H_2, which are assumed to be quasi-equilibrated in this analysis

$$NO\ (g) + * \rightleftharpoons NO^* \tag{10}$$

$$H_2\ (g) + 2^* \rightleftharpoons 2H^* \tag{11}$$

After adsorption of all required gas species, NO* is hydrogenated to HNO*

$$NO^* + H^* \rightarrow HNO^* \tag{12}$$

followed by hydrogenation to *HNOH*

$$HNO^* + H^* \rightarrow HNOH^* \tag{13}$$

and its dissociation

$$^*HNOH^* \rightarrow NH^* + OH^* \tag{14}$$

and any of these reactions may be reversible or irreversible and quasi-equilibrated or kinetically relevant.

For the maximum rate analysis, each quasi-equilibrated step can be written in terms of an equilibrium expression. For example, the adsorption of NO (eq 10) can be written in terms of the surface concentrations (in square brackets) and gas-phase pressures (in parentheses)

$$K_{NO} = \frac{[NO^*]}{(NO)[^*]} \tag{15}$$

where [*] represents the concentration of empty sites on the surface. Equilibrium constants can be computed from DFT-derived reaction free energies using the following equation

$$K = e^{-\Delta G_{rxn}/RT} \tag{16}$$

with rate constants (for kinetically relevant steps) computed from DFT-derived activation free energies

$$k = \frac{k_B T}{h} e^{-\Delta G_{act}/RT} \tag{17}$$

From these, a rate equation can be derived for every step independently by assuming that every preceding step is quasi-equilibrated. Each reaction pathway requires a total of two sites, and only two most abundant surface intermediates (MASI) are considered: NO* and H*, resulting in the same denominator for every rate expression.

The results of a maximum rate analysis on the formation and dissociation of HNOH* on Rh(111) surfaces at 423 K and 3 mbar NO are shown in Figure 11. These rates show, when examining pathway 5 in isolation, that HNO* hydrogenation to form HNOH* (step 5a) is the kinetically relevant step of pathway 5 on Rh(111). Pathway 5 can occur either through HNO* formation and hydrogenation (steps 3a and 5a) or through NOH* formation and hydrogenation (steps 4a and 5b). Compared to NO* hydrogenation, NOH* formation (step 4a) occurs with a higher maximum rate than HNO* formation (step 3a), and similarly, HNOH* formation from HNO* (step 5a) occurs with a higher maximum rate than from NOH* (step 5b). These parallel steps can be directly compared and demonstrate that routes via HNO* occur with higher rates than routes via NOH*. For the route via HNO*, the step that forms HNO* (step 3a) occurs with much higher maximum rates than the step that hydrogenates HNO* (step 5a), indicating that the former is quasi-equilibrated. Comparing HNOH* formation (step 5a) with HNOH* dissociation (step 5c) again shows that step 5a (formation) has the lower maximum rate, this indicates that it is the kinetically relevant step and HNOH* dissociation (5c) is a rapid irreversible reaction that follows. Increasing H_2 pressure increases the predicted maximum rates of all steps in this pathway, with H_2 kinetic orders depending on the number of H-atoms in each step; however, no lines cross over this wide H_2 pressure range (0.002−3 bar), indicating that the kinetically relevant step of pathway 5 does not change over this range of conditions. This results in a rate expression:

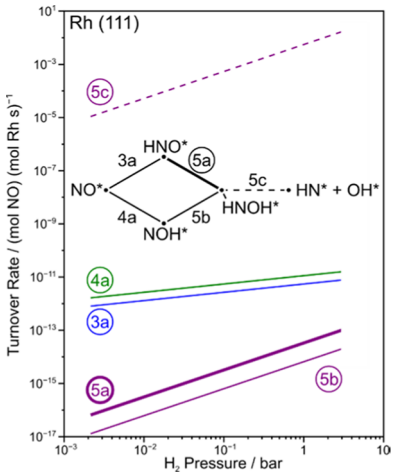

Figure 11. Maximum rate analysis and schematic representation of the formation and dissociation of HNOH* on Rh(111). P_{NO} = 0.003 bar, T = 423 K. Rate-determining step bolded. Colors and step numbers correspond to reaction pathways and steps in Scheme 1.

$$\frac{r_5}{[L]} = \frac{k_{5a}K_{3a}K_{H_2}K_{NO}(NO)(H_2)}{[1 + K_{NO}(NO) + K_{H_2}^{1/2}(H_2)^{1/2}]^2} \tag{18}$$

for pathway 5 with rate and equilibrium constants defined in Scheme 1. This rate expression for pathway 5 is first order in both NO and H_2 in the numerator and based on the surface coverages can predict many distinct kinetic regimes. The terms in the denominator denote relative abundances of empty sites, NO*, or H*. NO adsorption is more favorable than H_2 adsorption, even at these high NO* coverages, and thus DFT predictions suggest that the H*-term in the denominator can be neglected except at very high H_2/NO ratios (>10^3 or 10^4), similar to Pt. Equation 18 can be further simplified for NO*-covered surfaces to

$$\frac{r_5}{[L]} = \frac{k_{5a}K_{3a}K_{H_2}K_{NO}(NO)(H_2)}{[1 + K_{NO}(NO)]^2} \tag{19}$$

The filling calculations performed in Section 3.1 predict that the catalyst surfaces are saturated with NO* and that vacancies, while necessary for chemistry to occur, are not abundant (i.e., $K_{NO}(NO) \gg 1$ at all conditions). Because the surface is NO*-saturated, the rate equation for pathway 5 can be further simplified to

$$\frac{r_5}{[L]} = \frac{k_{5a}K_{3a}K_{H_2}(H_2)}{K_{NO}(NO)} \tag{20}$$

https://dx.doi.org/10.1021/acs.jpcc.0c04024
J. Phys. Chem. C 2020, 124, 13291−13303

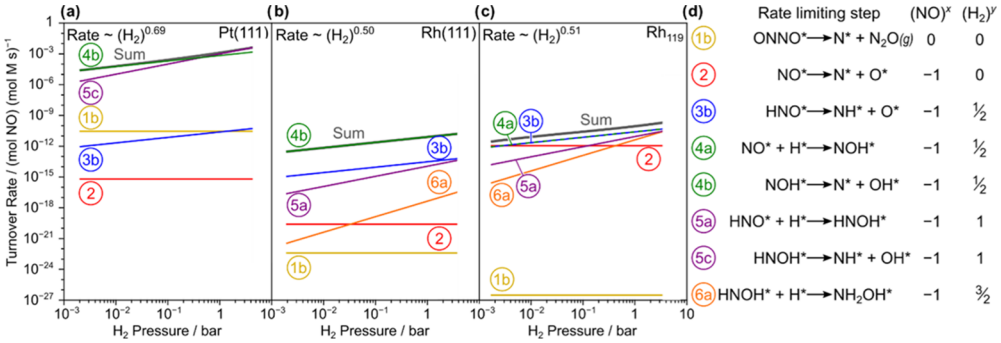

Figure 12. Maximum rate analysis showing the rate-limiting step for each NO cleavage pathway on (a) Pt(111), (b) Rh(111), and (c) Rh_{119} particles. (d) Rate-limiting steps and NO and H_2 pressure dependences for each pathway. steps 4a and 3b on Rh_{119} have identical rates. P_{NO} = 0.003 bar, T = 423 K. All rates on Pt were calculated from the previously reported barriers.[14]

Routes that cleave through HNO* (pathway 3) or NOH* (pathway 4) would follow a rate equation with a half-order dependence on H_2,i.e.,

$$\frac{r_i}{[L]}\frac{k_{ib}K_{ia}K_{H_2}{}^{1/2}(H_2)^{1/2}}{K_{NO}(NO)} \tag{21}$$

where K_{ia} is the equilibrium constant for the formation of either HNO* or NOH* (steps 3a and 4a, respectively) and k_{ib} is the rate constant for dissociation (steps 3b and 4b). Direct NO dissociation (pathway 2) is inhibited by NO and is zero order in H_2

$$\frac{r}{[L]} = \frac{k_2}{K_{NO}(NO)} \tag{22}$$

while NO-assisted activation (pathway 1) would be zero order in both H_2 and NO

$$\frac{r}{[L]} = k_{1b}K_{1a} \tag{23}$$

Maximum rate analyses were performed on every possible reaction for direct, NO-assisted, and H_2-assisted routes. Detailed analyses, such as the one performed for Figure 11, of each pathway on each system are available in the SI. Reactions on Pt surfaces tend to occur at higher rates than on Rh surfaces (Figure 12), consistent with experimental observations showing higher activity for Pt catalysts for NO−H_2 reactions.[64] The kinetically relevant step on Pt for each pathway is N−O scission (Figure 9a), while on Rh, the formation steps for HNOH* and H_2NOH* are limiting for pathways 5 and 6, but N−O cleavage is limiting in pathways 1−3. For pathway 4, NOH* dissociation (step 4b) limits the rate on Pt(111) and Rh(111), while on the Rh_{119}, half-particle NOH* formation (step 4a) limits the rates.

The NO activation mechanism changes at 0.6 bar H_2 on Pt(111) surfaces,[14] where the mechanism to activate NO changes from NOH* formation and dissociation (pathway 4) to HNOH* formation and dissociation (pathway 5) leading to a shift from half order to first order in H_2 pressure dependence. These two H_2-assisted routes are predicted to occur at many orders of magnitude higher than pathways 1−3, indicating the difficulty of direct or NO*-assisted NO activation pathways when even a small amount of H_2 is present.

NOH* formation and dissociation (pathway 4) is predicted to be the dominant NO consumption pathway on the Rh(111) model at all H_2 pressures, limited by NOH* dissociation. Reactions through NH_2OH, not considered on Pt, are unlikely to occur based on these predictions. All other pathways are >3 orders of magnitude slower than NOH* dissociation on Rh(111) (Figure 12b), resulting in predicted half-order dependence in H_2 and inhibition by NO at all relevant pressures.

The high NO* coverages on the Rh_{119} model (1.38 ML NO* with 1 ML on terraces) lead to strong coverage effects on the reactions occurring at the terrace of this model. NO-assisted NO activation is more difficult at high coverages, likely because that reaction exhibits a positive activation area: the transition state occupies more space on the catalyst surface than the pair of NO*, which it replaces in the thermochemical cycle reflected by the transition-state theory. Other routes involve NO* desorption as the first step, thus alleviating some of the strain in the high-coverage adlayer and generally reacting with higher rates on the particle model compared to the Rh(111) flat surface at 6/9 ML NO*. Direct NO dissociation (step 2) on Rh_{119} competes with H-assisted routes at low H_2 pressures (H_2/NO < 0.67 or < 2 mbar H_2), indicating that direct NO dissociation prevails over NO-assisted routes in the absence or near-absence of H_2 and in the absence of other reductants such as CO or hydrocarbons. Surface science observations suggest that direct NO* dissociation is completely inhibited at coverages >0.5 ML,[23] suggesting that particle curvature is responsible for increased rates of direct dissociation on Rh_{119}.

Both pathways 3 and 4 have identical rates on Rh_{119} as the transition states, which limit these pathways (those for steps 4a and 3b), have the same composition and the same effective free-energy barrier. Their effective enthalpy barriers, furthermore, are within 15 kJ mol^{-1} of one another, suggesting that temperature has a weak effect on their relative rates. One way to discern between these pathways would be to measure kinetic isotope effects (KIE). Observation of a primary KIE is consistent with the O−H bond formation occurring in step 4a, while a secondary KIE would be consistent with the N−O bond cleavage in step 3b. The kinetically relevant step for pathway 4 on Rh_{119} is NOH* formation (step 4a), indicating that this step is irreversible in all pathways that involve NOH*. This means that step 4a cannot be assumed to be quasi-equilibrated in the maximum rate analysis of pathways 5 or 6, as described in more detail in Section S4 of the SI. Pathway 5 then must occur through formation of HNO* (instead of NOH*) and is limited by the formation of *HNOH* from HNO* (step 5a), as shown in Figure 12c. At very high H_2 pressures (>3 bar, H_2/NO > 1000), pathways 3, 4, 5, and 6 all compete and are limited by hydrogenation steps, with higher

https://dx.doi.org/10.1021/acs.jpcc.0c04024
J. Phys. Chem. C 2020, 124, 13291−13303

H_2 pressures favoring pathways 5 and 6 as expected by their first- and 1.5-order H_2 dependencies in contrast to pathways 3 and 4, which are half order in H_2. These high H_2 pressures, however, are unlikely in exhaust gas because H_2 is primarily formed by dehydrogenation of uncombusted hydrocarbons, yielding negligible partial pressures.[10]

Predicted rates on Rh(111) surfaces and Rh_{119} half particles are similar, differing by only an order of magnitude, while the rates for ethane hydrogenolysis differ by 10^3−10^4 between the particle and surface models for Ir because ethane hydrogenolysis involves the replacement of surface-bound H* (the resting state and abundant surface species) with a CH−CH*‡ transition state. As coverage increases, the H* surface intermediate is weakly impacted, while the C_2H_2*‡ transition state is strongly destabilized, resulting in a large difference in the predicted rates.[33] Here, in contrast, the relevant competition is between the NO* adsorbate and a NH_xO*‡ (x = 0−2) transition state, which are much more similarly destabilized as coverage increases, resulting in milder impacts on absolute total rates. NO reduction rates on Rh are predicted to be ∼10^6× slower than rates on Pt (Figure 12). This large differences in the rates of Pt and Rh are supported by measured data, demonstrating that Rh has the same turnover rate at 475 K as Pt at 333 K for NO−H_2 reactions (at identical pressures);[13] this 142 K difference in the temperature is consistent with Pt being 10^5× more active than Rh, reasonably close to the DFT-predicted rate ratios.

4. CONCLUSIONS

NO dissociation through direct, NO-assisted, and H-assisted routes was considered on surface models of Pt and Rh at intermediate coverages as well as a fully covered Rh nanoparticle model that is more representative of practical catalysts. Surface models saturate at submonolayer coverages, with a coverage of 5/9 and 6/9 ML NO* on Pt(111) and Rh(111), respectively, above which NO binding free energies become positive. Curvature and undercoordinated sites on nanoparticles allow for supramonolayer coverages, leading to a total saturation coverage of 1.38 ML NO* on the Rh nanoparticle model, similar to H* chemisorption on Ir and Pt nanoparticles[36] and CO* on Ru.[37]

Direct and NO-assisted NO reduction routes are kinetically irrelevant on both Pt(111) and Rh(111) surface models. NO reduction, instead, occurs by H-assisted routes through the formation and subsequent dissociation of NOH* or HNOH* on Pt(111) surfaces; the mechanism shifts to that limited by HNOH* dissociation above 0.5 bar H_2 (0.003 bar NO, 423 K), consistent with the shift from half- to first-order H_2 dependence at high H_2/NO ratios.[14] In contrast, NO dissociation on Rh(111) is predicted to occur solely by the formation and subsequent dissociation of NOH*, leading to a half-order dependence on H_2 as measured.[15] For reactions on Rh_{119}, co-adsorbate interactions at high coverages destabilize transition states, which require adlayer restructuring and favor those which do not, resulting in more competition between dissociation pathways and a shifting mechanism as H_2 pressure changes. Direct NO dissociation occurs at very low H_2 pressures (<0.002 bar, H_2/NO < 0.67), yielding to H-assisted pathways (via NOH* and HNO* dissociations, which occur at identical rates) at intermediate H_2 pressures, while HNOH* formation and dissociation becomes the main pathway at high H_2 pressures (>3 bar, H_2/NO > 1000). These results suggest that isotopic studies of NO−H_2 reactions can give more insights into the key intermediates of NO activation on small supported Rh nanoparticle catalysts.

Rates on both Rh models were contrasted and compared with previously reported data on Pt surfaces. Overall rates on both Rh models are similar and are ∼10^6 times lower than rates on Pt, which agrees with differences in reaction temperatures of ∼140 K for the two metals.[13] The high reactivity of Pt toward NO−H_2 reactions, compared to Rh, is because Pt is better at hydrogenating NO and thus accelerates H-assisted NO activation reactions. This work suggests that H_2 formed at low pressures via hydrocarbon dehydrogenation or water gas shift reactions on three-way catalysts can reduce NO at Pt sites but is unlikely to reduce NO on Rh particles with those particles predominantly reducing NO via NO−CO reactions, which occur at higher rates than NO−H_2 reactions at automotive exhaust conditions.[12]

■ ASSOCIATED CONTENT

Supporting Information

The Supporting Information is available free of charge at https://pubs.acs.org/doi/10.1021/acs.jpcc.0c04024.

Information regarding frequency calculations and statistical treatments; minimum energy configurations of models at intermediate coverages; additional transition-state structures; additional comparisons of dissociation pathways on each system; and maximum rate analyses for each pathway (PDF)

■ AUTHOR INFORMATION

Corresponding Author

David Hibbitts − *Department of Chemical Engineering, University of Florida, Gainesville, Florida 32601, United States;* orcid.org/0000-0001-8606-7000; Email: hibbitts@che.ufl.edu

Authors

Pavlo Kravchenko − *Department of Chemical Engineering, University of Florida, Gainesville, Florida 32601, United States*

Varun Krishnan − *Department of Chemical Engineering, University of Florida, Gainesville, Florida 32601, United States*

Complete contact information is available at: https://pubs.acs.org/10.1021/acs.jpcc.0c04024

Notes

The authors declare no competing financial interest.

■ ACKNOWLEDGMENTS

This material is based upon work supported by the National Science Foundation under grant number CBET-1803165. Computational resources were provided by the Extreme Science and Engineering Discovery Environment (XSEDE), which is supported by the National Science Foundation grant number ACI-1548562. We acknowledge Hannes Simboeck, Enrique Iglesia, Andrew (Bean) Getsoian, and Phillip Christopher for their helpful technical discussions. Manuscript reviews and proofreading from Alexander Hoffman (University of Florida) and Abdulrahman Almithn (King Faisal University) are gratefully acknowledged.

■ REFERENCES

(1) Goldsmith, B. R.; Sanderson, E. D.; Ouyang, R.; Li, W.-X. CO- and NO-Induced Disintegration and Redispersion of Three-Way

Catalysts Rhodium, Palladium, and Platinum: An Ab Initio Thermodynamics Study. *J. Phys. Chem. C* **2014**, *118*, 9588−9597.
(2) Granger, P.; Parvulescu, V. I. Catalytic NO(x) Abatement Systems for Mobile Sources: From Three-way to Lean Burn After-treatment Technologies. *Chem. Rev.* **2011**, *111*, 3155−3207.
(3) Costa, C. N.; Savva, P. G.; Andronikou, C.; Lambrou, P. S.; Polychronopoulou, K.; Belessi, V. C.; Stathopoulos, V. N.; Pomonis, P. J.; Efstathiou, A. M. An Investigation of the NO/H2/O2 (Lean De-NOx) Reaction on a Highly Active and Selective Pt/La0.7Sr0.2-Ce0.1FeO3 Catalyst at Low Temperatures. *J. Catal.* **2002**, *209*, 456−471.
(4) Hahn, C.; Endisch, M.; Schott, F. J. P.; Kureti, S. Kinetic Modelling of the NOx Reduction by H2 on Pt/WO3/ZrO2 Catalyst in Excess of O2. *Appl. Catal., B* **2015**, *168−169*, 429−440.
(5) Kondarides, D. I.; Chafik, T.; Verykios, X. E. Catalytic Reduction of NO by CO over Rhodium Catalysts. *J. Catal.* **2000**, *193*, 303−307.
(6) Renzas, J. R.; Huang, W.; Zhang, Y.; Grass, M. E.; Somorjai, G. A. Rh1−x Pd x Nanoparticle Composition Dependence in CO Oxidation by NO. *Catal. Lett* **2011**, *141*, 235−241.
(7) Wang, L.; Zhang, S.; Zhu, Y.; Patlolla, A.; Shan, J.; Yoshida, H.; Takeda, S.; Frenkel, A. I.; Tao, F. (Feng). Catalysis and In Situ Studies of Rh_1/Co_3O_4 Nanorods in Reduction of NO with H_2. *ACS Catal.* **2013**, *3*, 1011−1019.
(8) Takahashi, N.; Shinjoh, H.; Iijima, T.; Suzuki, T.; Yamazaki, K.; Yokota, K.; Suzuki, H.; Miyoshi, N.; Matsumoto, S.; Tanizawa, T.; et al. The New Concept 3-way Catalyst for Automotive Lean-burn Engine: NOx Storage and Reduction Catalyst. *Catal. Today* **1996**, *27*, 63−69.
(9) Shen, H.; Shamim, T.; Sengupta, S. An Investigation of Catalytic Converter Performances During Cold Starts. In *SAE Technical Paper Series*; SAE International: 400 Commonwealth Drive, Warrendale, PA, 1999; Vol. *1*.
(10) Taylor, K. C. Nitric Oxide Catalysis in Automotive Exhaust Systems. *Catal. Rev.* **1993**, *35*, 457−481.
(11) Shelef, M.; Graham, G. W. Why Rhodium in Automotive Three-Way Catalysts? *Catal. Rev.* **1994**, *36*, 433−457.
(12) Kobylinski, T. P.; Taylor, B. W. The Catalytic Chemistry of Nitric Oxide. *J. Catal.* **1974**, *33*, 376−384.
(13) Chambers, D. C.; Angove, D. E.; Cant, N. W. The Formation and Hydrolysis of Isocyanic Acid During the Reaction of NO, CO, and H2 Mixtures on Supported Platinum, Palladium, and Rhodium. *J. Catal.* **2001**, *204*, 11−22.
(14) Hibbitts, D. D.; Jiménez, R.; Yoshimura, M.; Weiss, B.; Iglesia, E. Catalytic NO Activation and NO−H_2 Reaction Pathways. *J. Catal.* **2014**, *319*, 95−109.
(15) Hecker, W. Reduction of NO by H_2 over Silica-supported Rhodium: Infrared and Kinetic Studies. *J. Catal.* **1985**, *92*, 247−259.
(16) CPT Group GmbH. *Worldwide Emission Standards and Related Regulations*; Continental Automotive, 2019.
(17) Hirano, H.; Yamada, T.; Tanaka, K. I.; Siera, J.; Nieuwenhuys, B. E. The Reduction of Nitric Oxide by Hydrogen Over Pt, Rh and Pt-Rh Single Crystal Surfaces. In *New Frontiers in Catalysis*, Proceedings of the 10th International Congress on Catalysis, Budapest, 19−24 July 1992; Studies in surface science and catalysis; Elsevier: Amsterdam, 1993; pp 345−357.
(18) Hirano, H.; Yamada, T.; Tanaka, K. I.; Siera, J.; Cobden, P.; Nieuwenhuys, B. E. Mechanisms of the Various Nitric Oxide Reduction Reactions on a Platinum-rhodium (100) Alloy Single Crystal Surface. *Surf Sci* **1992**, *262*, 97−112.
(19) Burch, R.; Millington, P. J.; Walker, A. P. Mechanism of the Selective Reduction of Nitrogen Monoxide on Platinum-based Catalysts in the Presence of Excess Oxygen. *Appl. Catal., B* **1994**, *4*, 65−94.
(20) Kumar, A.; Medhekar, V.; Harold, M. P.; Balakotaiah, V. NO Decomposition and Reduction on Pt/Al2O3 Powder and Monolith Catalysts Using the TAP Reactor. *Appl. Catal., B* **2009**, *90*, 642−651.
(21) Frank, B.; Emig, G.; Renken, A. Kinetics and Mechanism of the Reduction of Nitric Oxides by H2 Under Lean-burn Conditions on a Pt−Mo−Co/α-Al2O3 Catalyst. *Appl. Catal., B* **1998**, *19*, 45−57.
(22) Bai, Y.; Mavrikakis, M. Mechanistic Study of Nitric Oxide Reduction by Hydrogen on Pt(100) (I): A DFT Analysis of the Reaction Network. *J. Phys. Chem. B* **2018**, *122*, 432−443.
(23) Borg, H. J.; Reijerse, J. F. C.-J. M.; van Santen, R. A.; Niemantsverdriet, J. W. The Dissociation Kinetics of NO on Rh(111) as Studied by Temperature Programmed Static Secondary Ion Mass Spectrometry and Desorption. *J. Chem. Phys.* **1994**, *101*, 10052−10063.
(24) Cobden, P. D.; Janssen, N. M. H.; van Breugel, Y.; Nieuwenhuys, B. E. Non-linear Behaviour in the NO—H2 Reaction over Rh(111). *Surf Sci* **1996**, *366*, 432−444.
(25) Schaak, A.; Imbihl, R. Spiral Waves and Formation of Low Work Function Areas in Catalytic NO Reduction with Hydrogen on a Rh(111) Surface. *J. Chem. Phys.* **2002**, *116*, 9021−9027.
(26) Makeev, A. G.; Slinko, M. M.; Janssen, N. M. H.; Cobden, P. D.; Nieuwenhuys, B. E. Kinetic Oscillations and Hysteresis Phenomena in the NO+H_2 Reaction on Rh(111) and Rh(533): Experiments and Mathematical Modeling. *J. Chem. Phys.* **1996**, *105*, 7210−7222.
(27) Wolf, R. M.; Bakker, J. W.; Nieuwenhuys, B. E. Dissociation of Nitric Oxide and Reaction with Hydrogen on Rh(111) and Various Stepped Rh(111) Surfaces. *Surf Sci* **1991**, *246*, 135−140.
(28) Costa, C. N.; Efstathiou, A. M. Transient Isotopic Kinetic Study of the NO/H_2/O_2(Lean de-NOx) Reaction on Pt/SiO_2 and Pt/La−Ce−Mn−O Catalysts. *J. Phys. Chem. B* **2004**, *108*, 2620−2630.
(29) Carré, S.; Dujardin, C.; Granger, P. Operando Infrared Spectroscopy of the Reduction of NO by H2 over Rhodium Based Catalysts. *Catal. Today* **2012**, *191*, 59−64.
(30) Huai, L.; Su, T.; Wen, H.; Jin, X.; Liu, J. NO Reduction by H_2 on the Rh(111) and Rh(221) Surfaces: A Mechanistic and Kinetic Study. *J. Phys. Chem. C* **2016**, *120*, 5410−5419.
(31) Ling, L.; Zhao, Z.; Feng, X.; Wang, Q.; Wang, B.; Zhang, R.; Li, D. Insight into the Reduction of NO by H_2 on the Stepped Pd(211) Surface. *J. Phys. Chem. C* **2017**, *121*, 16399−16414.
(32) Farberow, C. A.; Dumesic, J. A.; Mavrikakis, M. Density Functional Theory Calculations and Analysis of Reaction Pathways for Reduction of Nitric Oxide by Hydrogen on Pt(111). *ACS Catal.* **2014**, *4*, 3307−3319.
(33) Almithn, A.; Hibbitts, D. Effects of Catalyst Model and High Adsorbate Coverages in Ab Initio Studies of Alkane Hydrogenolysis. *ACS Catal.* **2018**, *8*, 6375−6387.
(34) Hendriksen, D. E.; Meyer, C. D.; Eisenberg, R. Nature of the Active Catalyst in the Rhodium Complex Catalyzed Reduction of Nitric Oxide by Carbon Monoxide. *Inorg. Chem.* **1977**, *16*, 970−972.
(35) Meyer, C. D.; Eisenberg, R. The Catalytic Reduction of Nitric Oxide by Carbon Monoxide Using dichlorodicarbonylrhodium(I) Anion. *J. Am. Chem. Soc.* **1976**, *98*, 1364−1371.
(36) Almithn, A. S.; Hibbitts, D. D. Supra-monolayer Coverages on Small Metal Clusters and Their Effects on H_2 Chemisorption Particle Size Estimates. *AIChE J.* **2018**, *64*, 3109−3120.
(37) Liu, J.; Hibbitts, D.; Iglesia, E. Dense CO Adlayers as Enablers of CO Hydrogenation Turnovers on Ru Surfaces. *J. Am. Chem. Soc.* **2017**, *139*, 11789−11802.
(38) Kresse, G.; Furthmüller, J. Efficient Iterative Schemes for Ab Initio Total-energy Calculations Using a Plane-wave Basis Set. *Phys. Rev. B: Condens. Matter* **1996**, *54*, 11169−11186.
(39) Kresse, G.; Furthmüller, J. Efficiency of Ab-initio Total Energy Calculations for Metals and Semiconductors Using a Plane-wave Basis Set. *Comput. Mater. Sci.* **1996**, *6*, 15−50.
(40) Kresse, G.; Hafner, J. Ab Initio Molecular-dynamics Simulation of the Liquid-metal-amorphous-semiconductor Transition in Germanium. *Phys. Rev. B: Condens. Matter* **1994**, *49*, 14251−14269.
(41) Kresse, G.; Hafner, J. Ab Initio Molecular Dynamics for Liquid Metals. *Phys. Rev. B* **1993**, *47*, 558−561.
(42) Kravchenko, P.; Plaisance, C.; Hibbitts, D.A New Computational Interface for Catalysis. 2019, preprint.
(43) Kresse, G.; Joubert, D. From Ultrasoft Pseudopotentials to the Projector Augmented-wave Method. *Phys. Rev. B* **1999**, *59*, 1758−1775.

https://dx.doi.org/10.1021/acs.jpcc.0c04024
J. Phys. Chem. C 2020, 124, 13291−13303

(44) Blöchl, P. E. Projector Augmented-wave Method. *Phys. Rev. B: Condens. Matter* **1994**, *50*, 17953−17979.
(45) Hammer, B.; Hansen, L. B.; Nørskov, J. K. Improved Adsorption Energetics Within Density-functional Theory Using Revised Perdew-Burke-Ernzerhof Functionals. *Phys. Rev. B* **1999**, *59*, 7413−7421.
(46) Perdew, J. P.; Burke, K.; Ernzerhof, M. Generalized Gradient Approximation Made Simple. *Phys. Rev. Lett.* **1996**, *77*, 3865−3868.
(47) Zhang, Y.; Yang, W. Comment on "Generalized Gradient Approximation Made Simple. *Phys. Rev. Lett.* **1998**, *80*, 890.
(48) Monkhorst, H. J.; Pack, J. D. Special Points for Brillouin-zone Integrations. *Phys. Rev. B* **1976**, *13*, 5188−5192.
(49) Jónsson, H.; Mills, G.; Jacobsen, K. W. Nudged Elastic Band Method for Finding Minimum Energy Paths of Transitions. In *Classical and Quantum Dynamics in Condensed Phase Simulations*; Berne, B. J.; Ciccotti, G.; Coker, D. F., Eds.; World Scientific: Singapore, 1998; pp 385−404.
(50) Henkelman, G.; Jónsson, H. Improved Tangent Estimate in the Nudged Elastic Band Method for Finding Minimum Energy Paths and Saddle Points. *J. Chem. Phys.* **2000**, *113*, 9978−9985.
(51) Henkelman, G.; Jónsson, H. A Dimer Method for Finding Saddle Points on High Dimensional Potential Surfaces Using Only First Derivatives. *J. Chem. Phys.* **1999**, *111*, 7010−7022.
(52) Herrmann, S.; Iglesia, E. Elementary Steps in Acetone Condensation Reactions Catalyzed by Aluminosilicates with Diverse Void Structures. *J. Catal.* **2017**, *346*, 134−153.
(53) Zhi, Y.; Shi, H.; Mu, L.; Liu, Y.; Mei, D.; Camaioni, D. M.; Lercher, J. A. Dehydration Pathways of 1-Propanol on HZSM-5 in the Presence and Absence of Water. *J. Am. Chem. Soc.* **2015**, *137*, 15781−15794.
(54) DeLuca, M.; Kravchenko, P.; Hoffman, A.; Hibbitts, D. Mechanism and Kinetics of Methylating C_6 −C_{12} Methylbenzenes with Methanol and Dimethyl Ether in H-MFI Zeolites. *ACS Catal.* **2019**, *9*, 6444−6460.
(55) Mei, D.; Lercher, J. A. Mechanistic Insights into Aqueous Phase Propanol Dehydration in H-ZSM-5 Zeolite. *AIChE J.* **2017**, *63*, 172−184.
(56) Almithn, A.; Hibbitts, D. Comparing Rate and Mechanism of Ethane Hydrogenolysis on Transition-Metal Catalysts. *J. Phys. Chem. C* **2019**, *123*, 5421−5432.
(57) Chen, B. W. J.; Mavrikakis, M. Effects of Composition and Morphology on the Hydrogen Storage Properties of Transition Metal Hydrides: Insights from PtPd Nanoclusters. *Nano Energy* **2019**, No. 103858.
(58) Hibbitts, D.; Neurock, M. Promotional Effects of Chemisorbed Oxygen and Hydroxide in the Activation of C−H and O−H Bonds over Transition Metal Surfaces. *Surf Sci* **2016**, *650*, 210−220.
(59) Cautero, G.; Astaldi, C.; Rudolf, P.; Kiskinova, M.; Rosei, R. A HREEL Investigation of Adsorption and Dissociation of NO on a Rh(110) Surface. *Surf. Sci.* **1991**, *258*, 44−54.
(60) Root, T. W.; Fisher, G. B.; Schmidt, L. D. Electron Energy Loss Characterization of NO on Rh(111). I. NO Coordination and Dissociation. *J. Chem. Phys.* **1986**, *85*, 4679−4686.
(61) Ho, P.; White, J. M. Adsorption of NO on Rh(100). *Surf. Sci. Lett.* **1984**, *137*, 103−116.
(62) Chin, Y.-H.; Buda, C.; Neurock, M.; Iglesia, E. Selectivity of Chemisorbed Oxygen in C−H Bond Activation and CO Oxidation and Kinetic Consequences for CH4−O2 Catalysis on Pt and Rh Clusters. *J. Catal.* **2011**, *283*, 10−24.
(63) Chin, Y.-H. C.; Buda, C.; Neurock, M.; Iglesia, E. Consequences of Metal-oxide Interconversion for C-H Bond Activation During CH4 Reactions on Pd Catalysts. *J. Am. Chem. Soc.* **2013**, *135*, 15425−15442.
(64) Dümpelmann, R.; Cant, N. W.; Trimm, D. L. The Positive Effect of Hydrogen on the Reaction of Nitric Oxide with Carbon Monoxide over Platinum and Rhodium Catalysts. *Catal. Lett* **1995**, *32*, 357−369.

https://dx.doi.org/10.1021/acs.jpcc.0c04024
J. Phys. Chem. C 2020, 124, 13291−13303